J Mater Sci (2008) 43:6967–6985
DOI 10.1007/s10853-008-2961-y

Processing methods to control silk fibroin film biomaterial features

Brian D. Lawrence · Fiorenzo Omenetto · Katherine Chui · David L. Kaplan

Received: 7 May 2008 / Accepted: 18 August 2008 / Published online: 17 September 2008

Abstract Control of silk structural and morphological features is reported for fibroin protein films via all aqueous processing, with and without polyethylene oxide (PEO). Silk films with thicknesses from 500 nm to 50 μm were generated with controllable surface morphologies by employing soft-lithography surface patterning or by adjusting PEO concentrations. FTIR analysis indicated that water-annealing, used to cure or set the films, resulted in increased β-sheet and α-helix content within the films. Steam sterilization provided an additional control point by increasing β-sheet content, while reducing random coil and turn structures, yet retaining film transparency and material integrity. Increased PEO concentration used during processing resulted in decreased sizes of surface globule structures, while simultaneously increasing uniformity of these features. The above results indicate that both surface and bulk morphologies and structures can be controlled by adjusting PEO concentration. The combined tool set for controlling silk film geometry and structure provides a foundation for further study of novel silk film biomaterial systems. These silk film biomaterials have potential applicability for a variety of optical and regenerative medicine applications due to their optical clarity, impressive mechanical properties, slow degradability, and biocompatibility.

Introduction

Silk proteins have proven to be remarkable biomaterials due to the combination of robust mechanical properties, biological compatibility, versatility in processing into many material formats, degradability by proteases [1, 2]. Silk fibroin has been studied for applications in the fields of tissue engineering and drug delivery [2–9] and provides a biocompatible matrix for in vivo applications [10–12]. Further, silk protein material degradation rates can be controlled based on processing conditions, which impact crystallinity [13–15]. Moreover, multiple material formats are available with silks, including films, fibers, sponges, and hydrogels, to provide versatility in uses [6, 13, 16–20]. Silk structures can be produced with defined material properties through control of β-sheet crystalline structure [16, 19, 21–25]. Silk films are a relatively simple format to generate and study via solution casting methods [16–18, 26], offering controllable material properties [18, 22, 23, 25, 27]. Thus, this material format provides a template upon which to elucidate the impact of processing variables on material features.

In the present study, silk films were surface patterned using an adapted soft-lithography casting technique [28, 29]. Surface patterning is a useful method for forming nano- and microscaled structures on silk film surfaces. These surfaces can be used to direct cellular responses, such as alignment, or to control the deposition of extracellular matrix [30–34]. Currently, these techniques have been applied for various biomaterials, such as hyaluronic acid (HA), collagen, and polytlactic acid (PLA) [31, 35, 36]. However, silk offers a combination of features that cannot be matched by these other biodegradable polymers. These features include enhanced surface patterning resolution with the additional benefit of highly controlled material properties, transparency, and robust mechanical features [2, 29]. In addition, silk processing can be conducted in an all-aqueous approach under ambient temperature conditions.

B. D. Lawrence · F. Omenetto · K. Chui · D. L. Kaplan (✉)
Department of Biomedical Engineering, Tufts University,
4 Colby St., Medford, MA, USA
e-mail: David.Kaplan@tufts.edu

Previously, silk films from hundreds of microns to <500 nm were formed [7, 17, 18], and a broader range of such features were explored in the present study. These types of films would offer potential utility for a variety of biological applications, such as in the design of lamellar tissue structures, biosensor platforms, or drug delivery systems [9, 29, 36]. Silk films can also be processed to produce water-insoluble films that can be surface patterned with high resolution (<20 nm) and incorporated with bioactive moieties for enhanced functionalization [18, 29]. In addition, fibroin film structure is impacted by the presence of polyethylene oxide (PEO) during processing, due to phase separation [17]. The resulting bulk and surface features may be useful as bioactive interfaces to stimulate desired cellular responses [32, 33, 37–41]. Furthermore, PEO is leached from the silk film matrix to generate defined porous structures [17, 24]. These porous structures may be utilized to enhance nutrient diffusion, provide filtration, or improve cellular communication through the silk film matrix.

The goal of the present study was to expand the understanding and control of silk film morphological and structural features, mainly focusing on pore structure and surface patterns. The aim was to provide a route to the generation of a wider range of silk film material features to enhance options for these films in cell and tissue studies, as well as in other broader material science applications, such as for sensors and membrane separation tools. Toward this goal, a systematic study was performed in which the use of PEO to control morphology was studied. Control of pore structure and of bulk and surface features of these films was gained through this phase separation approach, resulting in new options for the generation of silk-based biomaterials with predictable structure and morphology.

Materials and methods

Preparation of silk solution

As previously reported [18], *Bombyx mori* silk cocoons were cut into four and boiled for 40 min in 0.02 M Na_2CO_3 (Sigma–Aldrich) to extract the glue-like sericin proteins from the structural fibroin proteins. The fibroin extract was then rinsed three times in dH_2O for 20 min per wash. The rinsed fibroin extract was dissolved in 9.3 M LiBr solution at room temperature, and then left to sit covered in a 60 °C oven for 4 h. The solution was dialyzed against dH_2O (MWCO 3,500, Pierce, Inc.) for 48 h. The silk solution was then centrifuged twice at 13,000*g* for 20 min each. The final concentration of aqueous silk solution was 8 wt./vol.% which was determined by weighing the remaining solid after drying 1 mL of aqueous solution over night at 60 °C.

Preparation of PDMS substrates

PDMS substrates with a range of 0.5 to 1.0 mm thicknesses were prepared by casting 3.5 mL of a 9:1 mixture of PDMS potting solution to catalyst blend on a 5 × 5 cm square polystyrene surface. PDMS grooved substrates were produced by casting 3.5 mL of the same 9:1 blend onto a 5 × 5 cm optical grating, with 600, 1,200, 2,400, and 3,600 lines/mm groove spacings. Cast PDMS negatives were inspected using a Zeiss LEO 982 scanning electron microscope (SEM) operating at an accelerating voltage of 5 kV. The cast PDMS solution was then allowed to degas for 2-h under vacuum, and then cured in an oven at 60 °C overnight. The following day the cured PDMS was removed from the substrates and cut into round geometries with 14 mm diameters. These PDMS substrates were placed cast side up, and prepared for silk casting by rinsing with 70% ethanol with three subsequent dH_2O washes to remove any particulates. The same PDMS surfaces were used for multiple castings, and preliminarily cleaned with 9.3 M LiBr solution before each silk film casting to remove any silk residue.

Preparation of surface patterned silk films

Silk films of 50 μm thicknesses were cast upon flat and the various surface patterned PDMS surfaces using 100 μL of 8 wt./vol.% silk fibroin solution. The cast silk solution was covered with a venting lid and allowed to dry overnight. Once dried, the films were water-annealed by placing the samples within a water filled desiccator and with a 25 in. Hg vacuum for 6 h. This water-annealing technique produces a water-insoluble and transparent film post-processing [18, 26]. Each silk film sample was then removed from the PDMS substrate. Atomic force microscopy (AFM) was used to determine groove depth and surface roughness of the patterned silk films. Images of the film samples were acquired with a Digital Instrument Dimension 3100 (Veeco Instruments, Inc., Woodbury, NY) in tapping mode. Images were taken in air, flattened, and plane fitted as required.

Preparation of silk films with variable thickness

Silk films with variable thicknesses were prepared by casting 100 μL of different silk solution concentrations upon flat and patterned 14 mm diameter PDMS substrates. Cast percent weight aqueous silk solutions were: 8.0, 5.0, 2.50, 2.0, 1.75, 1.5, 1.25, 1.0, 0.75, 0.5, and 0.25 wt./vol.%. For each concentration, 12 film samples were produced on flat PDMS surfaces. Cast silk solutions were covered with a venting lid and allowed to dry. Once dried, the cast films were water-annealed and the post-water-annealed films were placed in 100% methanol (MeOH) for 30 s to allow

for successful film removal from the respective PDMS substrates. The films were removed and then placed in a water bath for 5 min to rinse away remaining MeOH, and then set aside to dry.

Silk film thickness measurement and analysis

The film samples were flash frozen in liquid nitrogen, and then cracked down the center using a razor blade. The films were then mounted for SEM analysis with their cross-sectional surface facing up. The samples were sputter coated with a 40 nm coating of gold using a Polaron SC502 Sputter Coater (Fisons, VG Microtech, East Sussex, England). The cross-sectional area of the various film thicknesses were then imaged using SEM. Three images from each silk film sample were taken for a total of 36 cross-sectional images per silk concentration group. Film thickness was measured using ImageJ analysis software [42]. Film sample measurements were combined for each silk concentration. A random sample set of 30 measurements was selected and statistical analysis was performed for each sample set using Microsoft Excel. For each concentration group, a sample mean and standard deviation was calculated, graphed, and a best-ft curve was applied. One-way ANOVA was performed across separate film silk concentration groups. For post hoc analysis, Student *t*-tests were performed to determine statistical significance between groups ($p < 0.05$).

Preparation of steam sterilized silk films

Silk films, 30 μm thick, were cast on round PDMS surfaces using 100 μL of 8% silk solution. The cast silk solutions were covered with a venting lid, and allowed to dry overnight. Once dried, the films were split into four groups of three, and each group was processed under different conditions. The first group was not processed and used as an untreated control. Two groups were water-annealed for 6 h, in which one of the two groups was steam sterilized ($T = 121$ °C, $P = 15$ psi, $t = 25$ min). Water-annealing was performed by placing the silk film samples within a water-filled desiccator and pulling a 25 in. Hg vacuum for 5 h. The final group was steam sterilized using the same conditions as above after drying. Following sterilization, each silk film sample was removed from the respective PDMS substrate and dried. The final four processing conditions analyzed were: untreated, water-annealed, steam sterilization, and water-annealed with steam sterilization.

FTIR analysis of silk fibroin secondary structure

Silk film secondary structural analysis was measured using an FTIR spectrometer. Spectral scans were obtained using dried samples from each processing condition. For each sample, a measurement of 66 scans was collected at a resolution of 4 cm^{-1}, which was acquired over a wavenumber range of 400–4,000 cm^{-1}. Spectral manipulations were performed with OPUS (Version 5.5 software, Bruker Optics, Inc.). Quantification of silk secondary structure was based on analyzing the amide I region (1,600–1,700 cm^{-1}) [43]. Background absorption due to water was subtracted from the sample spectra to obtain a flat recording in the range of 1,750–2,000 cm^{-1} [44]. The amide I region (1,600–1,710 cm^{-1}) was selected from the entire spectrum, and a linear baseline was applied to the spectrum.

Deconvolution was carried out using 12 fixed fitting peak values as cited previously [22, 25]. To confirm that each fitting peak position represented a real spectral signal signature from the silk film sample, second derivative analysis was performed on spectra from each processing condition. Second derivative analysis was carried out using a third degree polynomial function with a 9-point Savitski-Golay smoothing function [44, 45]. During the deconvolution process, the peak positions were held constant for each sample to enable future comparisons between processing groups for protein secondary structure content. A Levenberg–Maquardt function available in the program was used for initial curve fitting. The curve fit was then refined using a local least squares fit, and the peak positions were reset to their initial positions if needed. The Levenberg–Maquardt function was used again for a final fit refinement. Throughout the process, the deconvoluted peak shapes were assumed to be Lorentzian [19]. The average percent composition of fibroin secondary structure for the series of samples [21, 22], specifically the amount of β-sheet structure, was assessed by integrating the area of each deconvoluted curve and then normalizing to the total area of the amide I region of the fitted spectra.

Statistical analysis of FTIR data

Deconvoluted FTIR data were analyzed to determine average secondary protein secondary structure content from each set of samples ($n = 3$) for the various processing conditions. The means and standard deviations were calculated for each sample set. ANOVA and Student *t*-tests were performed to determine statistical differences between the sample set means for various comparison tests.

Porous silk film preparation and surface feature analysis

Various PEO ($M_v = 900{,}000$) concentrations (0, 0.05, 0.10, 0.15, 0.20, and 0.25 wt./vol.%) were mixed with 1% silk solution. Six film samples of each mixed solution were then cast using the above film preparation method on both flat and surface patterned substrates. An additional three

silk films with no PEO were cast for surface feature characterization purposes. After water-annealing, the films were then placed into a water bath for PEO leaching over a 24 h time period at ambient temperature conditions. The films were placed in a MeOH bath, and then in a water bath for 5 min for rinsing. Silk films were removed from the water bath and placed onto glass cover slips with the desired viewing surface of the film facing up. Three film samples per viewing surface were prepared. The films were then dried on cover slips, which allowed for attachment of the silk films to the glass surface. The silk films were sputter coated with gold and imaged using SEM at a 5 kV acceleration voltage.

Statistical analysis of silk film pore size distribution

SEM images were analyzed using ImageJ software [46], and statistical analysis was performed using Microsoft Excel to identify surface features and individual feature sizes for each PEO concentration and casting surface. For total surface area calculations, one image from each silk film PEO concentration and casting side ($n = 3$) was analyzed using the manual trace tool in ImageJ. Total surface area was calculated by summing all feature size surface areas within a 50 × 50 μm image area. For feature size calculations, three silk film samples were analyzed for each PEO concentration and casting surface (PDMS and air interfaces). A total of 50 surface features were counted from one representative image for each sample using the manual trace tool in ImageJ, and 25 values were randomly selected using Excel. Sample means and standard deviations were calculated. The collected feature sizes were then log-normalized to produce a normal distribution of data. Data analysis was performed by one-way ANOVA and Student *t*-tests for post hoc comparisons. Statistical significance was considered for $p < 0.05$.

Cross-sectional analysis of silk film bulk thickness

Silk films with varying PEO concentrations (0, 0.05, 0.16, 0.31, 0.58, and 0.61) were prepared as previously described on both flat and patterned PDMS surfaces. For each concentration, 2 and 20 μm thick films were cast for imaging. Three silk film samples were prepared for each PEO concentration and thickness determined as above—films were frozen and cracked in liquid nitrogen, mounted for cross-sectional and surface viewing, and sputter coated with 30 nm of gold for SEM imaging. The cross-sectional thicknesses from four of the silk film groups (0.16, 0.31, 0.58, and 0.61% PEO) ($n = 3$) were evaluated for feature size surface area using the ImageJ manual trace tool ($n = 20$). Sample means and standard deviations were calculated. The collected feature sizes were then log-normalized. Data analysis was performed by one-way ANOVA and Student *t*-tests for post hoc comparisons. Statistical significance was considered for $p < 0.05$.

Results and discussion

Film fabrication, surface patterning, and controlled film thickness

Silk films offer robust mechanical properties and all-aqueous materials processing [18]. In addition, the ability to interface silk with biological systems may allow for their use in a number of biomedical and environmental applications. Therefore, a solution casting method was employed for surface patterning that generated transparent silk optical devices through a soft-lithographic technique (Fig. 1a) [28]. These films were produced by casting the aqueous silk solution on patterned hydrophobic PDMS substrates. Negative molding casts of diffractive grating surfaces were produced using a PDMS soft-lithography process. These surfaces possessed 600, 1,200, 2,400, and 3,600 lines/mm aligned grooved features. Optical mirror surfaces served as substrates in the process to generate flat surfaces. Silk solutions were cast on the various PDMS surfaces to produce silk films with both flat and patterned surfaces (Fig. 1b and c). AFM was used to characterize each surface (Fig. 1d and e), and root-mean-square (RMS) values were calculated to determine surface roughness. Decreased surface feature size resulted in a decrease in surface roughness, with RMS values below 1 nm for films cast on flat PDMS molds prepared from the mirror surfaces.

The low surface roughness for the silk film surfaces indicated the ability of the fibroin protein to form high resolution patterned features. Silk fibroin is a structural protein employed by arthropods for external structures such as webs and cocoons [47]. The structure of this protein has been optimized for tight packing into beta sheet crystals to maximize stability in the environmental as well as mechanical functions in prey capture or housing [7, 48]. Therefore, the silk protein readily adopts to a geometrical shape even at the nanoscale, as demonstrated on the flat silk film surface, due to chain packing and stabilization during self-assembly (Fig. 1d). Localized RMS values indicate surface patterning resolution within the single nanometer range.

Similar surface patterning results were reported using 1-butyl-3-methylimidazolium chloride (BMIC) ionic liquid solution [34]. However, the present methodology is an all-aqueous process and does not require methanol for film formation and stabilization. These features are advantageous for the inclusion of labile molecules, such as proteins, organisms, and DNA, among others.

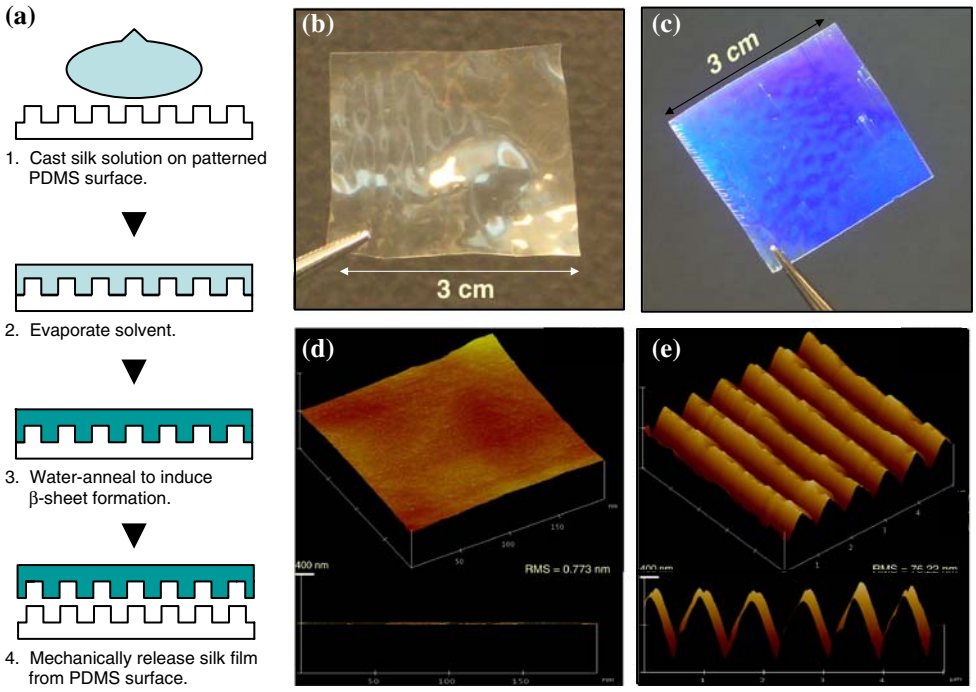

Fig. 1 (**a**) Schematic of silk film soft-lithography casting methodology in which silk solution is cast on patterned PDMS substrates, the silk is then dried and processed to induce β-sheet formation, and then the silk film is mechanically removed from the PDMS substrate retaining a negative image of the casting surface. Images of silk films with (**b**) flat and (**c**) diffraction patterned surface, with respective AFM images of topography shown below (**d**, **e**). Both surface and cross-sectional topographic views are shown with respective RMS values shown as insets

Water-annealing processing may be also be advantageous for biomedical applications, where residuals from an ionic liquid solution may be problematic for biological systems [49]. In addition, the present method for film formation is accomplished through solvent evaporation, and is highly controllable for control of film dimensions, morphology, and structure. The crystalline content of the films can be controlled using multiple post-casting processes, [17, 18, 24], a feature that is difficult to achieve when methanol is used to induce beta sheet formation in the films [16].

Silk fibroin film thickness was controlled by varying silk solution concentration while using a constant PDMS casting surface area and solution volume. Films as thin as 500 nm and as thick as 40 μm were produced using various silk solution concentrations. Silk films were water-annealed to induce the formation of the β-sheet crystalline structure [18, 24, 25]. Water insoluble transparent silk films are generated by this process that possess increased mechanical strength [18, 26].

This casting method provided repeatable silk film cross-sectional thicknesses based on SEM analysis, and the measured silk film mean thickness (SD, $n = 30$) increased with increasing silk solution concentration (Fig. 2). A linear curve was fit ($R^2 = 0.99$) to the silk film mean thicknesses. The results indicate that silk solution concentration is the primary contributing factor for thick film formation using the above casting technique.

Drying effects play a significant role in silk fibroin thin film formation by inducing β-sheet formation [7]. These

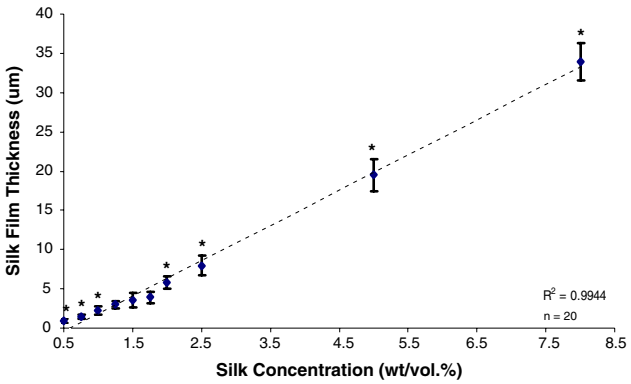

Fig. 2 Cast silk film thickness as a function of fibroin solution concentration with linear curve fit. Casting volume and casting surface area were held constant at 100 μL and 14 mm diameter, respectively. * Indicates statistical significance between adjacent sample group means ($p < 0.05$; error bars = 95% confidence intervals)

previous results indicated that silk fibroin secondary structure may play a role in thin film thickness formation. Such drying effects may impact the non-linear thin film portion of the fitted curve above (Fig. 2). Such non-linear effects may be attributed to the fact that increased β-sheet formation generates a more tightly packed structure between fibroin molecules [50]. This increased packing may decrease film thickness formation. Further studies must be carried to assess this relationship between silk fibroin secondary structure and thin film thickness.

FTIR characterization of silk film fibroin protein secondary structure

Spectral deconvolution was used to quantify protein secondary structure content for each processing condition. Second derivative analysis of the amide I region of the FTIR spectrum for untreated and water-annealed conditions was performed using OPUS software (v.5.5, Bruker, Inc.) to locate spectral signatures. Spectral signatures for each processing condition were denoted by the lowest curve peaks corresponding with second derivative analysis (Fig. 3a and b) [25]. A total of 12 peaks for unprocessed silk films were detected (Fig. 3a). The presence of the 12 peaks corresponded with previous results from the literature, indicating the location of the resonance frequencies for various fibroin secondary structures within the amide I region [22]. The water-annealed films exhibited a total of 13 peaks with an uncharacteristic peak at 1,654 cm^{-1} (Fig. 3b). Second-derivative analysis has not been previously reported for water-annealed silk films; therefore this peak may be characteristic of this processing method which falls on the cusp of random coil and α-helical regions for the silk fibroin [22, 25]. The corresponding silk fibroin protein secondary structures for the FTIR spectra are shown in Table 1. The secondary protein structures consisted of side chains (1,605–1,615 cm^{-1}), *β*-sheets (1,619–1,628 and 1,697–1,703 cm^{-1}), random coil (1,638–1,655 cm^{-1}), α-helix (1,656–1,662 cm^{-1}), and turns (1,663–1,696 cm^{-1}) [22, 25].

Deconvolution was performed using a 12-peak fitting process, in which initial fixed peak locations were assigned to the central region for each of the 12 secondary protein structure regions as indicated in Table 1 [25]. Side chains were located at 1,611 cm^{-1}, *β*-sheets were located at 4

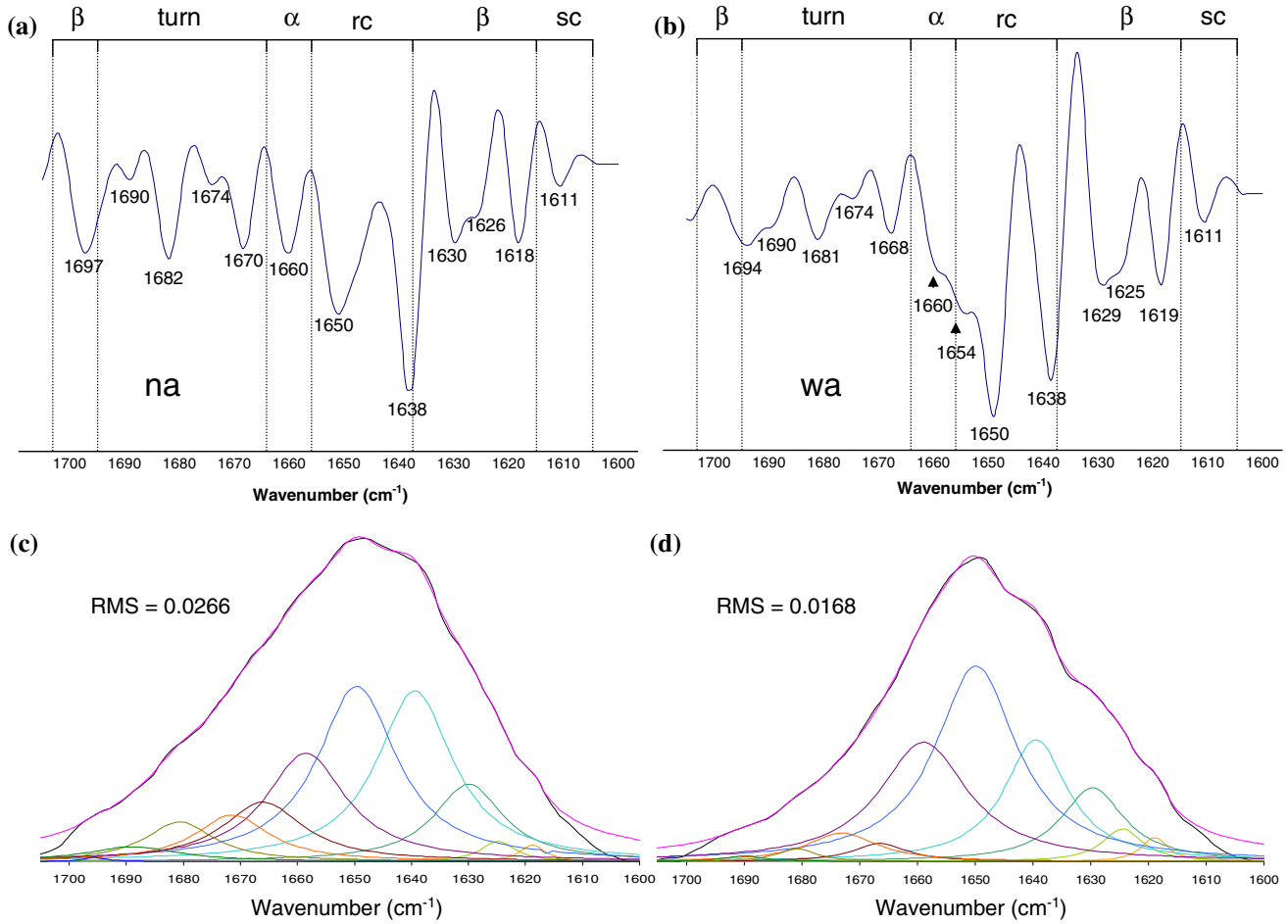

Fig. 3 Second derivative analysis of FTIR spectra for (**a**) untreated and (**b**) water-annealed silk films. Protein secondary structure regions are shown at the top of each spectrum in which side chains locations are between 1,605 and 1,615 cm^{-1}; *β*-sheet locations are between 1,616 and 1,637 and 1,697 and 1,703 cm^{-1}; random coil locations are between 1,638 and 1,655 cm^{-1}; α-helix locations are between 1,656 and 1,662 cm^{-1}; and turn structure locations are between 1,663 and 1,695 cm^{-1}. Deconvoluted FTIR curves for (**a**) untreated and (**b**) water-annealed silk films. The blue curve represents the original FTIR spectrum, the pink curve represents the spectral fit, and 12 deconvoluted curves are shown below. The RMS value for each curve fit is shown as an inset

Table 1 Vibrational band assignments for the amide I region of silk fibroin [22, 25]

Wavenumber range (cm^{-1})	Secondary structure assignment
1,605–1,615	(Tyr) side chains/aggregated strands
1,616–1,621	Aggregate β-strand/sheet (weak)[a]
1,622–1,627	β-Sheets (strong)[a]
1,628–1,637	β-Sheets (strong)[b]
1,638–1,646	Random coils/extended chains
1,647–1,655	Random coils
1,656–1,662	α-Helix
1,663–1,670	Turns
1,671–1,685	Turns
1,686–1,695	Turns
1,697–1,703	β-Sheets (weak)[a]

[a] Intermolecular β-sheets; [b] Intramolecular β-sheets

positions (1,619, 1,624, 1,630, and 1,698 cm^{-1}), random coils were located at 1,640 cm^{-1}, α-helix was located at 1,650 and 1,659 cm^{-1}, and turns were located at four positions (1,666, 1,674, 1,680, and 1,691 cm^{-1}). A Levenberg–Maquardt function was used for curve fitting (Fig. 3c and d) [19, 25]. RMS values for the fitted curves were 0.0168–0.0266 for untreated and water-annealed films, respectively. The reported RMS error was comparable to other curve fitting methods described in the literature [19, 22, 25, 43–45, 51]. Throughout the process, the deconvoluted peak shapes were assumed to be a Lorentzian distribution as this gave the best fit, and has been used in previous studies for silk fibroin [19, 22, 25, 43, 44, 51]. Following deconvolution, the respective areas underneath each component curve were integrated and then divided by the total area under the amide I region fitted spectrum to give a normalized percent content value of silk fibroin secondary structure [19, 22, 25, 43, 44, 51].

Average values of fibroin secondary structure content are given with their standard deviations (SD) in Table 2. Curve-fitting procedures may add a level of error to overall signal detection. Prior to deconvolution, second derivative analysis indicated the existence of the 12 peaks for each processing condition. This is an indicator that actual protein secondary structure spectral signatures were measured for each processing condition. Results from this method appeared to give accurate estimates of overall secondary structure content as indicated by the relatively small sample SDs. This indicates minimal observed spectrum-to-spectrum variation between component bands for similar samples sets ($n = 3$). Additionally the relatively low RMS values provide evidence that an acceptable fit was achieved for the deconvoluted spectra. It should be noted that water-annealing exhibited a 13th peak, which may be a source for experimental error during the deconvolution process. However, water-annealing exhibited the lowest RMS value amongst groups, which may indicate the associated extra peak error may be negligible.

The percent content of silk secondary structures was quantified and then statistically analyzed to draw comparisons between different processing conditions (untreated and water-annealed) for both flat and 1.67 μm and 833 nm grooved surfaces (0, 600, and 1,200 lines/mm, respectively) (Table 2). β-sheet content increased, with statistical significance, after water-annealing for all surfaces (Fig. 4a). This change also corresponded with statistically significant decrease in turn structure for all samples surfaces. Additionally, α-helical content was found to statistically increase between processing conditions for 0 and 1,200 lines/mm samples. Random coil content did not statistically change between processing conditions for all silk film surfaces. These results indicate that water-annealing methods increase both β-sheet and α-helical content, which is compensated for by a decrease in turn structure content. In addition, random coil structures appear to be minimally affected by the water-annealing process. Random coil content is substantially decreased using other silk film processing methods such as MeOH treatment [16].

Significant differences were also found between silk film surfaces with similar processed samples ($n = 3$) (Fig. 4a). For water-annealed conditions, a decrease in β-sheet content was observed for 1,200 lines/mm film surfaces when compared to 600 lines/mm surfaces. These results correspond with a significant increase in random coil content for 1,200 lines/mm film surfaces when compared to the 600 lines/mm pattern for water-annealing conditions. No change in α-helical or turn structure content

Table 2 Silk secondary content for various untreated and water-annealed film surfaces

Silk secondary structure	Non-treated (% content ± SD; $n = 3$)			Water-annealed (% content ± SD; $n = 3$)		
	Flat	600 lines/mm	1,200 lines/mm	Flat	600 lines/mm	1,200 lines/mm
β-Sheet	11.94 ± 0.27	11.73 ± 0.78	10.20 ± 1.47	19.47 ± 3.65	21.06 ± 0.93	14.74 ± 1.12
Random coil	50.99 ± 1.01	48.67 ± 0.49	51.02 ± 0.94	51.17 ± 3.09	47.64 ± 0.44	53.54 ± 1.91
α-Helix	12.39 ± 0.91	14.64 ± 1.81	12.93 ± 0.71	16.28 ± 1.02	15.86 ± 1.71	16.54 ± 0.91
Turns	24.68 ± 0.46	24.96 ± 2.55	25.86 ± 1.68	13.03 ± 0.53	15.34 ± 1.00	15.18 ± 0.20

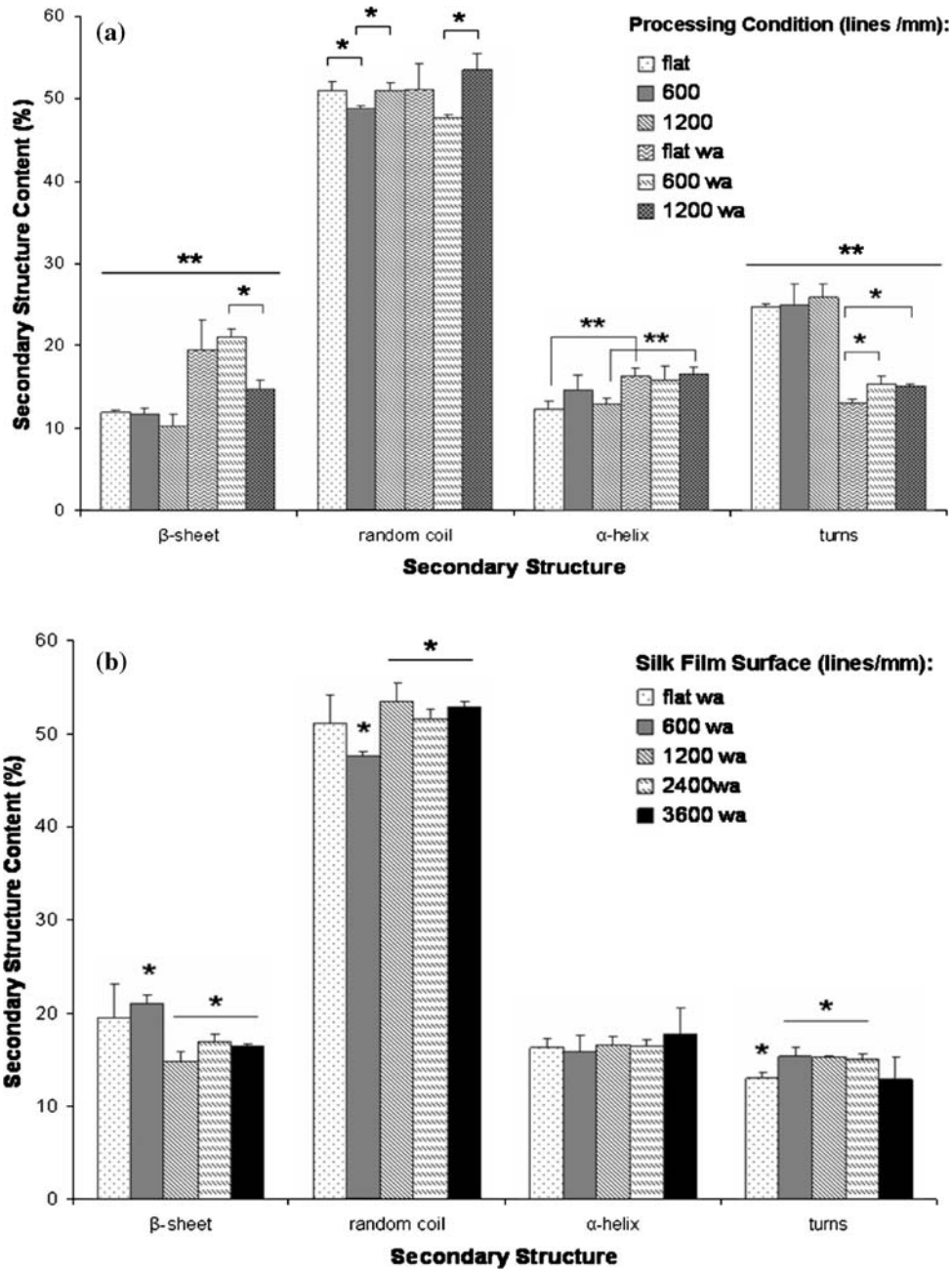

Fig. 4 Silk fibroin secondary structure content for various silk film processing conditions. (**a**) Secondary structure content for untreated and water-annealed silk films with flat and patterned (600 and 1,200 lines/mm) surfaces. Water-annealing increased both β-sheet and α-helix content, while simultaneously decreasing turn structure content. Statistical significance indicated by * for between groups of similar processing, and ** for between groups of different processing ($n = 3$; $p < 0.05$; error bars = SD). (**b**) Secondary structure content for water-annealed films with varying surfaces. Surface patterns greater then 600 lines/mm influenced β-sheet formation, while stabilizing random coil content. Statistical significance indicated by * ($n = 3$; $p < 0.05$; error bars = SD)

was found for water-annealing conditions between 1,200 and 600 lines/mm surfaces. However, a significant decrease in turn content was found for the flat silk film surfaces when compared to patterned silk surfaces. When comparing untreated samples, there was a significant decrease in random coil content when compared to both flat and the 1,200 lines/mm pattern. No other significant changes in secondary structure were detected for the untreated samples. These results demonstrate that the 1,200 lines/mm surface pattern impacts β-sheet formation to some degree and stabilizes the random coil structures during the water-annealing process.

To further explore these phenomenon, water-annealed silk films with 417 and 278 nm groove patterned surfaces (2,400 and 3,600 lines/mm) were produced. FTIR spectra were taken for each sample set ($n = 3$), and the fibroin secondary structure components were analyzed using the above spectral deconvolution method. This experiment was undertaken to determine how the presence of surface features affects β-sheet formation during the water-annealing process. Statistical comparison between groups indicated that the 600 lines/mm pattern had greater β-sheet content when compared to 1,200, 2,400, and 3,600 lines/mm patterns (Fig. 4b). No statistical differences were detected

between the flat and patterned surfaces. A complimentary effect was exhibited for random coil structure content, in that random coil content decreased for the 600 lines/mm surface pattern when compared to 1,200, 2,400, and 3,600 lines/mm surfaces. No statistical difference was exhibited between flat and patterned surfaces. No statistical differences were found for α-helical content, but a significant increase in content of turn structures was found for 600, 1,200, and 2,400 lines/mm patterned surfaces when compared to flat surfaces.

The above results indicate that patterned surfaces do not affect the formation of fibroin β-sheet secondary structure pre-water-annealing, as shown from the deconvolution data (Fig. 4a). However, the presence of the silk surface pattern significantly affects β-sheet, random coil, and turn secondary structure formation within the silk film bulk (Fig. 4a). Furthermore, the sizes of the patterned features also exhibit a significant effect on secondary structure formation post-water-annealing of the silk films (Fig. 4b). Smaller and denser surface features (1,200, 2,400, and 3,600 lines/mm) decreased β-sheet formation while simultaneously increasing random coil formation. The presence of these smaller and denser surface features inhibited the formation of β-sheets during water-annealing, while stabilizing the presence of random coil structures. However, such effects were not present for the 600 lines/mm patterning, which shows similar secondary structure content to flat film surfaces. The mechanism responsible for these effects is currently unclear, although aspects of surface interactions and/or templating may play a role. The degree of secondary structure formation may be related to an increase in surface energy exhibited by the 1,200, 2,400, and 3,600 lines/mm patterns.

Water-annealing processing has been suggested to allow relatively slow β-sheet crystal formation, as opposed to other crystallizing methods such as MeOH treatment, where rapid dehydration is promoted [18]. Therefore, surface effects on secondary structure formation may become more apparent with lower rate of secondary structure transition, as exhibited by water-annealing. Another possible explanation may be due to silk fibroin high surface patterning resolution, as demonstrated above. Thus, the silk fibroin may interact with the 1,200, 2,400, and 3,600 lines/mm PDMS surfaces in such a way that stabilizes the random coil structure while depressing β-sheet formation throughout the silk film bulk. Again, surface energies and interactions may play a role here.

At this point it is not understood why the changes in surface patterning affected protein secondary structure. The prospect of controlling secondary structure formation through surface-induced interactions may find functional use when designing for specified degradation rates or for a targeted biological surface interaction. However, the extent to which this feature can be controlled is not clear. Further experiments using time-resolved spectroscopy techniques [52, 53] may help to elucidate the kinetics of structure formation during the water-annealing process, which may lead to more insight into such secondary structure formation mechanisms and the role of surface features on this process.

Silk secondary structure of water-annealed and steam sterilized films

Sterilization is an important aspect to medical device design when generating materials for implantation. Sterilization methods must meet two criteria: (1) microbial disinfection of the medical device material and (2) uncompromised material integrity post-sterilization. Steam sterilization is a common disinfecting method in both research and industrial capacities due to ease of processing, accessibility, and wide acceptance for clinical and research needs. Steam sterilization would also be a useful method for sterilizing silk films. The caveat to steam sterilization is that it subjects a material to 121 °C, saturated humidity, and 15 psi of pressure. Recent studies exploring temperature effects on silk films have shown that an increase in β-sheet content corresponds with increased casting temperature [22, 25]. Similar results have also been observed for silk hydrogels in which an increased rate in β-sheet formation has been observed at elevated gelation temperatures [19]. It has also been shown that humidity plays a role in fibroin secondary structure, in which increased humidity increases secondary structure formation [18, 27, 54]. It is also known that silk materials withstand temperatures above 200 °C without significant change in structure or modulus.

FTIR spectroscopy was used to determine changes in silk fibroin protein secondary structure with respect to the various post-cast processing methods, including water-annealing, steam sterilization, water-annealing with steam sterilization, and no post-cast processing. Spectral deconvolution and statistical comparisons were drawn between processing groups. Both water-annealing and steam sterilization had significant impact on secondary structure, especially with regard to increased β-sheet content. The amide I (1,600–1,700 cm^{-1}) and amide II (1,500–1,600 cm^{-1}) regions for various processed samples are shown in Fig. 5. Initial examination of the spectral curves indicates an amide I peak shift after steam sterilization. Dominant peaks were observed in the amide I region at 1,648 and 1,649 cm^{-1} for unprocessed and water-annealed fibroin films, respectively (Fig. 5c and d). Samples steam sterilized with and without prior water-annealing exhibited amide I peaks located at 1,622 and 1,623 cm^{-1}, respectively (Fig. 5a and b). Similar shifts in the FTIR amide I

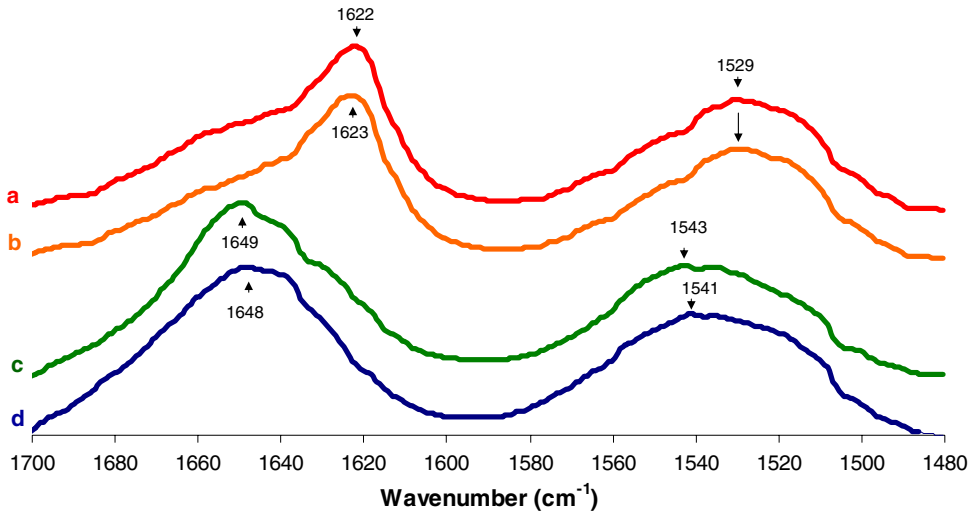

Fig. 5 Comparative FTIR spectra of amide I (1,600–1,700 cm^{-1}) and amide II (1,500–1,600 cm^{-1}) regions for silk fibroin films produced using various processing conditions: (**a**) water-annealing with steam sterilization, (**b**) steam sterilization, (**c**) water-annealing, and (**d**) no processing. The *y*-axis indicates arbitrary intensity values. Shifts in the amide I and amide II regions after post-steam sterilization result from increased β-sheet content and decreased amorphous silk structures

spectrum have been previously demonstrated with methanol and isothermal heat annealing treatments. Such shifts indicate increased silk II β-sheet content with a simultaneous reduction of silk I structures that give rise to bands in the range of 1,640–1,660 cm^{-1} region [16, 22, 25, 43, 44, 55].

A second peak shift in the amide II region of the FTIR spectrum was also demonstrated after steam sterilization. Dominant peaks located at 1,541 and 1,543 cm^{-1} with unprocessed and water-annealed samples, respectively (Fig. 5c and d). Steam sterilization samples with and without water-annealing demonstrated an amide II peak shift at 1,529 cm^{-1} (Fig. 5a and b). This peak shift corresponds with increasing β-sheet and reduced silk I structure [56]. The amide I and amide II peak shifts demonstrate that steam sterilization increases silk fibroin β-sheet structure content.

Spectral deconvolution was used to quantify protein secondary structure for each processing condition. Second derivative analysis indicated the existence of the 12 peaks for each processing condition (Fig. 6a and b). Silk film secondary structure content for each processing method was determined by deconvoluting the amide I region (Fig. 6c and d) [19, 25, 43, 45]. Average values of fibroin secondary structure content are given with their standard deviations (SD) in Table 3.

The water-annealed samples exhibited higher β-sheet content when compared to untreated and steam sterilized samples (Fig. 7). A corresponding statistical difference in the decrease of random coil structures is also observed for both steam sterilizing sample groups when compared to untreated and water-annealed samples. The decrease in random coil structure was greater for water-annealed samples with steam sterilization when compared to steam sterilized samples alone. However, this was not the case between untreated and water-annealed samples in which a statistical difference was not observed. A statistical difference was not observed for α-helical structure content between steam sterilization processing groups, although this structure content was significantly less in the steam sterilized samples when compared to untreated and water-annealed silk films. However, water-annealed samples showed a significant increase in α-helix content when compared to untreated samples. Additionally, turn structure content was significantly reduced for all processed samples when compared to untreated samples. No significant difference in turn structure content was detected between steam sterilization groups.

The above results indicate that steam sterilization induces a dramatic increase in total β-sheet content, which appears similar to previously reported β-sheet content values for methanol treatment [19, 25]. Amorphous silk I structure content (i.e., random coil, α-helix, and turn structures) for steam sterilized groups decreased in proportion to increased β-sheet formation when compared to untreated samples. However, water-annealing alone did not show this same relationship when compared to untreated samples. Random coil content did not decrease significantly between water-annealed and untreated silk film samples, while the α-helical content significantly increased after water-annealing when compared to untreated samples. Furthermore, a significant decrease in turn structure was seen after water-annealing when compared to untreated films. Therefore, it is likely that increased β-sheet and α-helical structure content is compensated primarily by decreased turn content after water-annealing. When comparing overall structure content between water-annealed and untreated films the percent β-sheet and α-helix content increase corresponds to the percent turn decrease (Fig. 7).

The above comparisons between different silk film processing conditions provide insight into the mechanism of β-sheet formation within the silk film matrix. Before

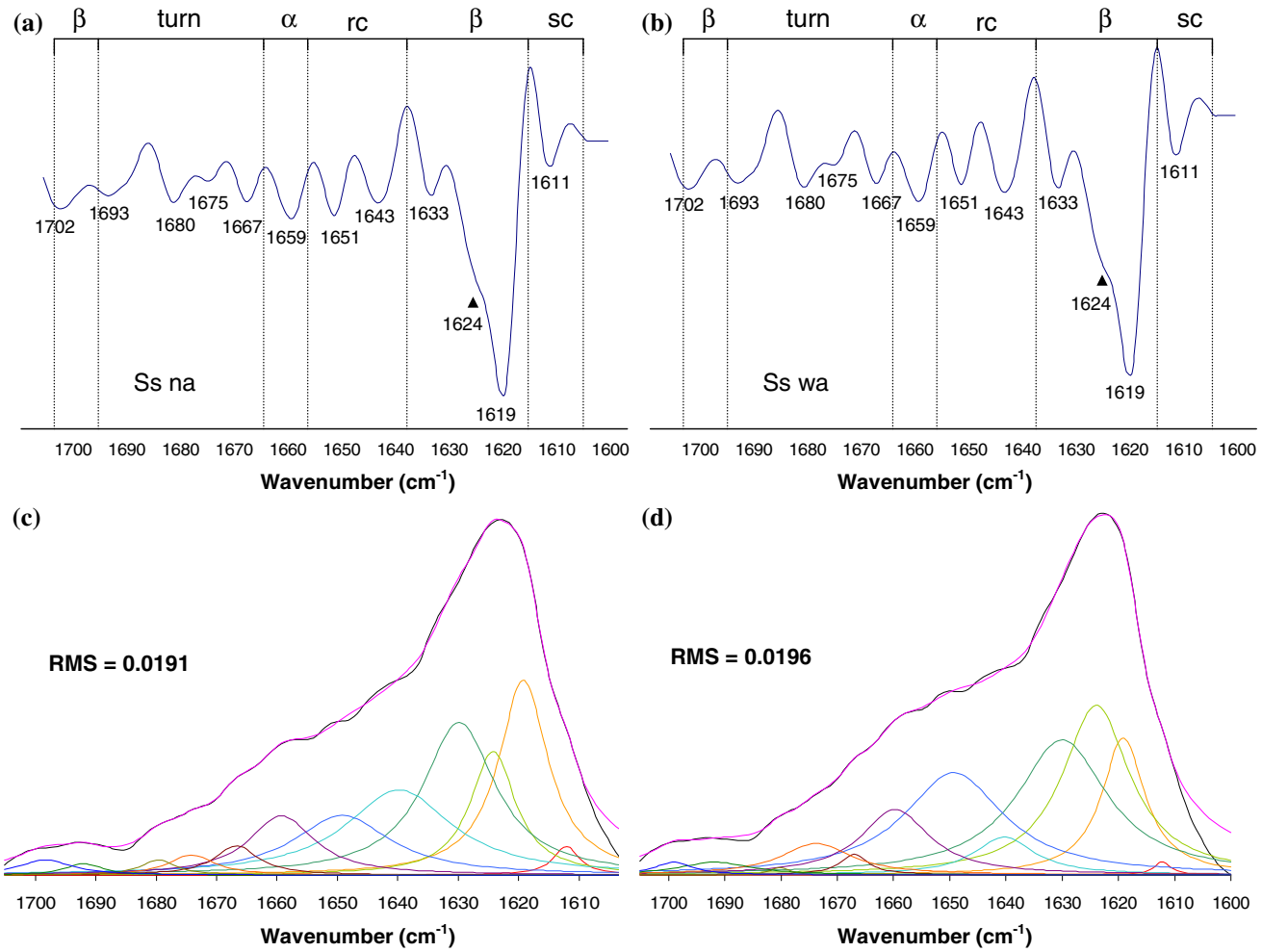

Fig. 6 Second derivative analysis of FTIR spectra for (**a**) steam sterilized and (**b**) water-annealing with steam sterilization silk films. Protein secondary structure regions are shown at the top of each spectrum in which side chains locations are between 1,605 and 1,615 cm^{-1}; β-sheet locations are between 1,616 and 1,637 and 1,697 and 1,703 cm^{-1}; random coil locations are between 1,638 and 1,655 cm^{-1}; α-helix locations are between 1,656 and 1,662 cm^{-1}; and turn structure locations are between 1,663 and 1,695 cm^{-1}. Deconvoluted FTIR spectra for each silk film processing condition: (**a**) steam sterilization and (**b**) water-annealing with steam sterilization. The *y*-axis indicates arbitrary intensity. RMS values for each curve fit are shown as insets. Original spectrum is shown in black and fitted curve is denoted in pink. Each of the 12 deconvoluted curve components is shown underneath

processing, the majority of the silk film matrix is composed of amorphous silk I structures (88%). Upon water-annealing, there is an 11% decrease in turn structures, with a corresponding 6% increase in β-sheet and 5% increase in α-helical structures (Fig. 7). These results indicate that the turn structure is the first silk I structure to become reduced in route to silk II transformation [48].

These structural changes may be explained by the increase of molecular movement of the silk fibroin chains which is induced by the absorption of water molecules during the water-annealing process. Silk fibroin has been shown to possess a decreased glass transition temperature (T_g) with increasing water absorption.[23, 27]. Dehydrated silk fibroin possesses a T_g of 178 °C which decreases to below 40 °C at 75% relative humidity [27]. This substantial depression in T_g has been attributed to water molecules behaving as a plasticizer to allow greater intermolecular movement between fibroin protein chains [54]. The increased chain movement permits the formation of more thermodynamically stable secondary structures (i.e., β-sheets and α-helices). The increase in α-helical structure content after water-annealing indicates that this structure may be an intermediate between silk I and silk II structure formation. It has been shown that hydrophobic environments promote α-helix formation [57].

Subjecting the silk fibroin films to elevated temperature, humidity, and pressure during steam sterilization promotes β-sheet crystallization. The effect that steam sterilization exhibits on the formation of the silk fibroin protein secondary structures has not been reported previously. Furthermore, it has not been demonstrated how elevated environmental pressure, as exhibited during steam

Table 3 Individual and total average values for silk fibroin film secondary structure content ($n = 3$)

Silk secondary structure	Wavenumber (cm^{-1})	% Protein secondary structure content (SD, $n = 3$)							
		None	Total	Water-annealed	Total	Steam sterilized	Total	Combined	Total
Side chains	1,611	0.00	0	0.01 ± .01	0	1.40 ± 0.11	1.40 ± 0.1	0.48 ± 0.06	0.48 ± 0.06
β-Sheets	1,619	0.9 ± 0.4	12.0 ± 1.0	2.6 ± 1.1	17.6 ± 2.9	20.6 ± 1.0	54.7 ± 1.2	13.4 ± 2.0	58.3 ± 1.1
	1,624	1.5 ± 0.1		3.3 ± 0.3		10.2 ± 1.1		21.1 ± 1.3	
	1,630	9.4 ± 1.2		11.5 ± 2.5		22.4 ± 0.2		23.1 ± 0.9	
	1,698	0.2 ± 0.1		0.2 ± 0.4		1.5 ± 0.2		0.8 ± 0.2	
Random coil	1,640	24.3 ± 0.4	50.8 ± 1.7	16.6 ± 0.9	50.0 ± 3.6	16.9 ± 1.4	29.7 ± 1.2	6.1 ± 1.8	23.4 ± 0.8
	1,650	26.6 ± 1.7		33.5 ± 3.5		12.7 ± 1.0		17.4 ± 2.5	
α-Helix	1,659	17.2 ± 2.6	17.2 ± 2.6	23.4 ± 2.4	23.4 ± 2.4	7.3 ± 0.9	7.3 ± 0.9	10.0 ± 2.2	10.0 ± 2.2
Turns	1,666	7.8 ± 1.1	20.0 ± 2.5	2.1 ± 0.5	9.0 ± 1.6	2.4 ± 0.3	6.9 ± 1.0	0.9 ± 0.3	7.8 ± 1.1
	1,674	4.9 ± 1.6		4.2 ± 0.2		2.5 ± 0.6		5.2 ± 1.4	
	1,680	4.9 ± 0.4		1.7 ± 1.2		0.8 ± 0.2		0.2 ± 0.1	
	1,691	2.5 ± 0.2		1.0 ± 0.4		1.3 ± 0.5		1.6 ± 0.1	

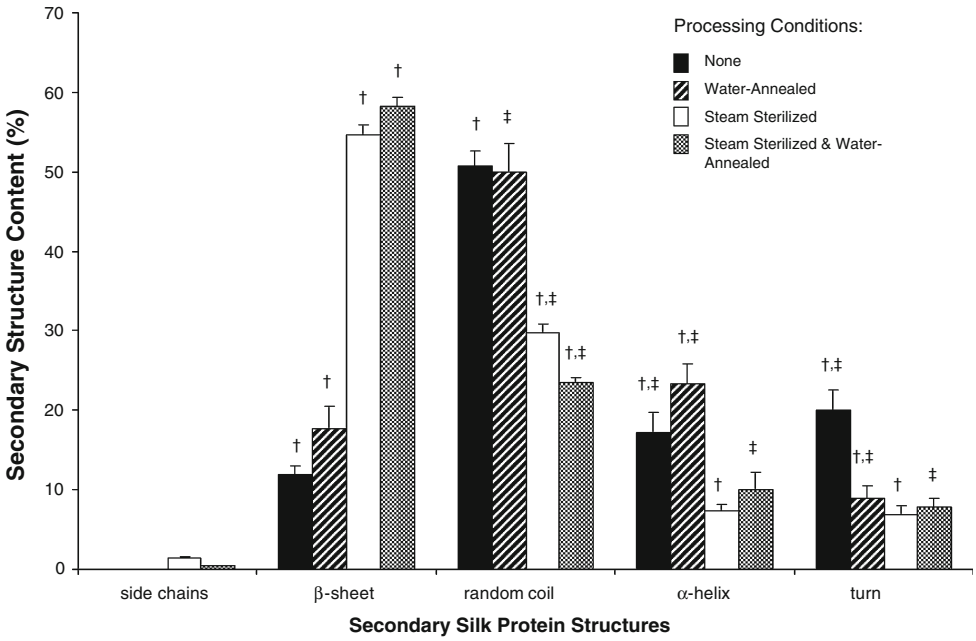

Fig. 7 Silk protein secondary structure content for four different film processing conditions. Statistical analysis was carried out using ANOVA followed by post hoc Student *t*-tests between comparative groups († and ‡ indicate $p < 0.05$ between sample set means, $n = 3$, and error bars = SD)

sterilization, will affect silk fibroin secondary structure. It has been shown that applied hydrostatic pressure to synthetic polymers increases the elastic modulus by increasing crystalline structure content [58–60]. Similarly, the β-sheet crystalline structure appears to be induced to a greater extent under the pressurized processing of steam sterilization. After steam sterilization, β-sheet formation substantially increases to above 50% total silk film content. This is balanced by the simultaneous decrease in silk I amorphous structures. The random coil secondary structure exhibits the largest decrease in structure content with 20% and 25% reduction for steam sterilized and water-annealed with steam sterilization groups, respectively, when compared to untreated samples.

There is an approximate 10% reduction in α-helical content for both steam sterilized groups when compared to untreated samples. In addition, turn structures exhibit an approximate 13% decrease in structure content for steam sterilized groups when compared to untreated samples. The saturated vapor environment will contribute to decreasing the T_g of silk fibroin, as shown previously in the literature.[27, 54] The decreased T_g combined with elevated temperatures will contribute to increased fibroin chain movement. In addition, the increased environmental pressure within the sterilization chamber contributes to an increased rate of fibroin polymer chain interactions. These factors combined will likely increase the transition rate from the silk I to the more energetically favorable silk II

state, thereby promoting more β-sheet formation. This is demonstrated by the large increase in β-sheet content for both steam sterilization groups (Fig. 7). The reduction of α-helical structure content for both steam sterilization groups is an expected outcome due to the fact that this structure is less energetically favorable then the β-sheet structure. Although α-helical structures increased during water-annealing with the increasing hydrophobic environment, the additional energy input from both the elevated temperature and atmospheric pressure would make the β-sheet conformation more favorable. These results infer further that the α-helical structure may act as a β-sheet intermediate within the silk film bulk.

When the various structure signals were separated and statistically compared, differences between means were seen to exist between the different chemical signal resonances for the different protein secondary structures of different processing conditions. For unprocessed and water-annealed fibroin film samples, the only statistical increase in β-sheet content was seen at 1,624 cm^{-1}, which is a strong spectral signature for intermolecular β-sheet formation (Fig. 8a) [22, 25]. These results suggest that water-annealing promotes intermolecular β-sheet formation. In addition, random coil signatures statistically decreased at 1,640 cm^{-1} but statistically increased at 1,650 cm^{-1}. The increase in random coil content at 1,650 cm^{-1} may be more representative of increased α-helical content due to the close signal spectral signatures of these two structures, which are commonly combined as silk I in other studies [7, 16, 19, 56]. The various turn structure resonances were also significantly affected by water-annealing. Decreased turn content was seen at 1,666, 1,680, and 1,691 cm^{-1} for water-annealed samples when compared to unprocessed samples (Fig. 8e). Thus, turn structure seems to be uniformly decreased upon water-annealing.

For steam sterilized samples, β-sheet spectral signatures varied between steam sterilization groups (Fig. 8b). These

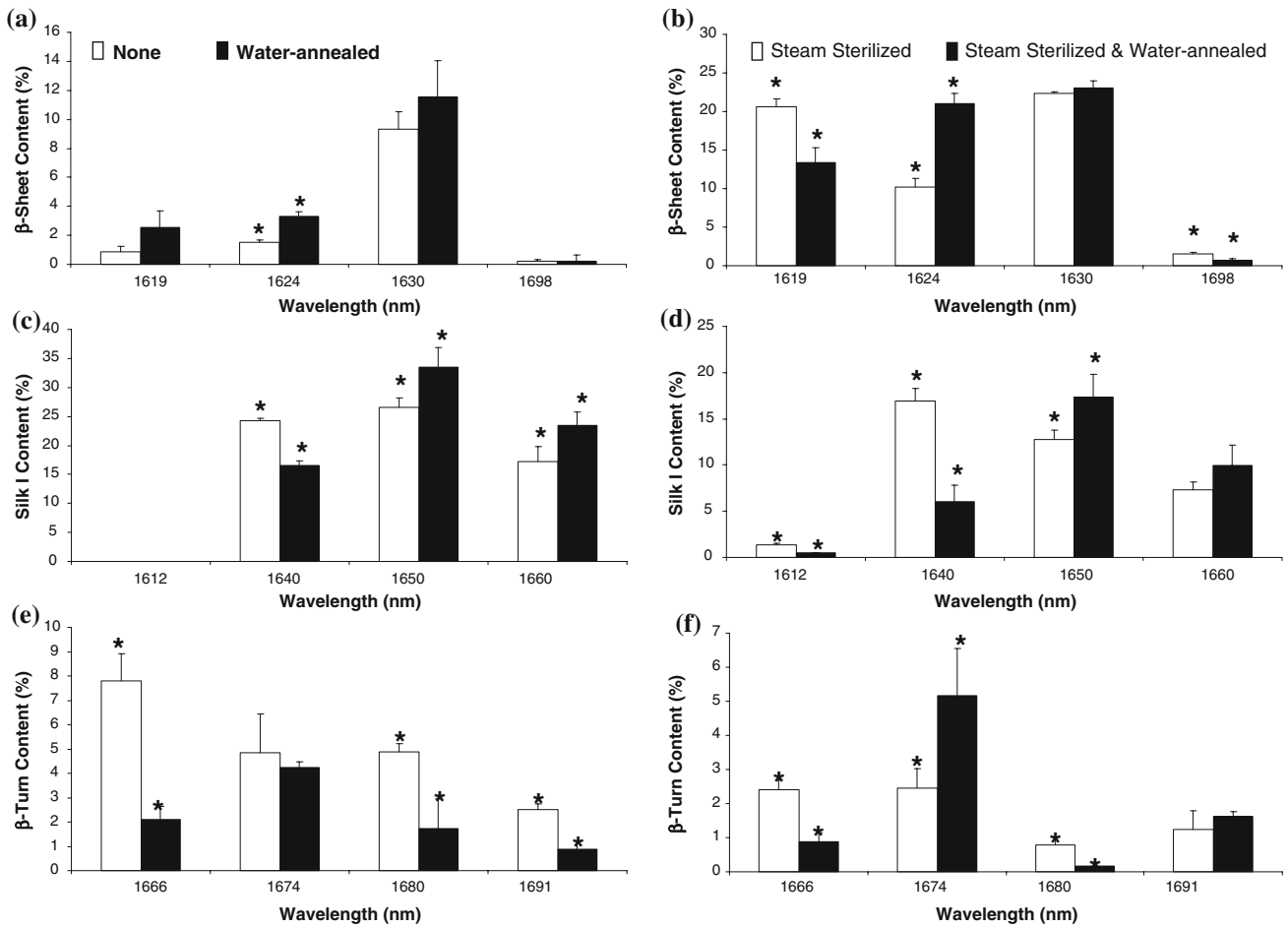

Fig. 8 Comparative silk fibroin protein secondary structure spectral frequencies for different processing methods. Respective comparisons between unprocessed and water-annealed samples and between steam sterilized and water-annealed with steam sterilization samples for (**a** and **b**) β-sheets, (**c** and **d**) side chains, random coils and α-helix, and (**e** and **f**) turn structures. Statistical differences were found between sample groups (* indicates $p < 0.05$, $n = 3$, and error bars = SD)

results indicate that the aggregate β-strand signal (1,619 cm^{-1}) significantly decreased for water-annealed films with steam sterilization when compared to steam sterilized films alone. Additionally, the spectral signature for intermolecular β-sheet associations (1,624 cm^{-1}) statistically increased for water-annealed films with steam sterilization when compared to steam sterilized films. These results indicate that increased intermolecular β-sheet association occurs for water-annealing with steam sterilization treatment when compared to steam sterilization treatment alone. This effect appears to be derived from the water-annealing treatment. This is indicated by the similar results found when comparing water-annealed to unprocessed films.

The spectral signatures for the random coil structures for both steam sterilized samples draw similarities from their non-sterilized counterparts (Fig. 8d). Water-annealing with steam sterilization shows a significant decrease in the 1,640 cm^{-1} band and a significant increase in the 1,650 cm^{-1} band when compared to steam sterilized samples. As in the untreated and water-annealed samples the increase at 1,650 cm^{-1} may be due to increased α-helical content. Changes are also apparent for β-turn secondary structures in that significant decreases are seen at both the 1,666 and 1,680 cm^{-1} bands. Such decreases were also found when comparing untreated to water-annealed samples. In addition, there was a significant increase observed at the 1,674 cm^{-1} band. This band has historically been contributed to either turn or β-sheet spectral signatures depending on the cited study [21, 22, 25, 51]. However, in this study, the 1,674 cm^{-1} band signature showed a statistical increase with both water-annealing and steam sterilization treatment, which may indicate that this band is an indicator for β-sheet signal. A schematic summarizing the proposed silk fibroin protein secondary structure changes during the different processing modalities are presented in Fig. 9.

Control of silk film surface feature size/density by PEO addition

The addition of PEO to silk solutions induces a phase separation [17, 24]. In the present study, PEO and silk solutions were cast on PDMS surfaces, were allowed to dry, were water-annealed, and then were left to sit within a water bath for 24 h in ambient conditions. SEM imaging revealed changes in surface topography depending on PEO concentration (Fig. 10). Surface features were formed after PEO leaching in a water bath for 24 h [17]. Following this incubation period, void structures were formed within the

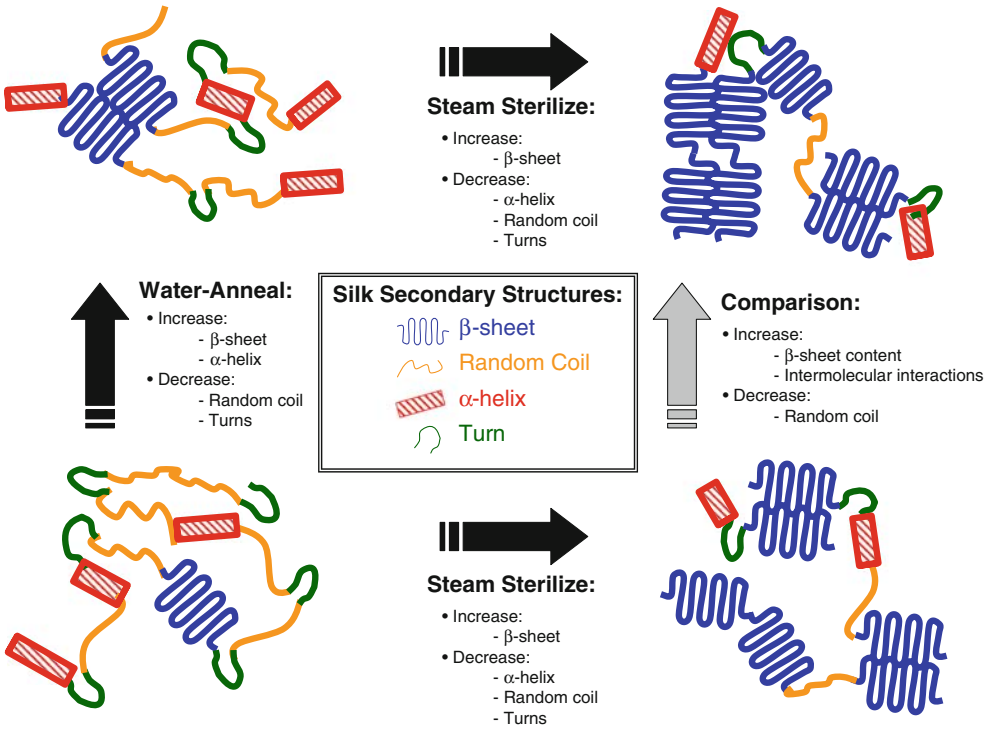

Fig. 9 Schematic diagram illustrating the silk protein secondary structural changes exhibited during water-annealing and steam sterilization processing. Arrow indicates changed structure post-processing. A comparison is shown between steam sterilization with and without prior water-annealing (gray arrow). Denoted increases and decreases refer to water-annealed with steam sterilized processing as compared to steam sterilization processing alone

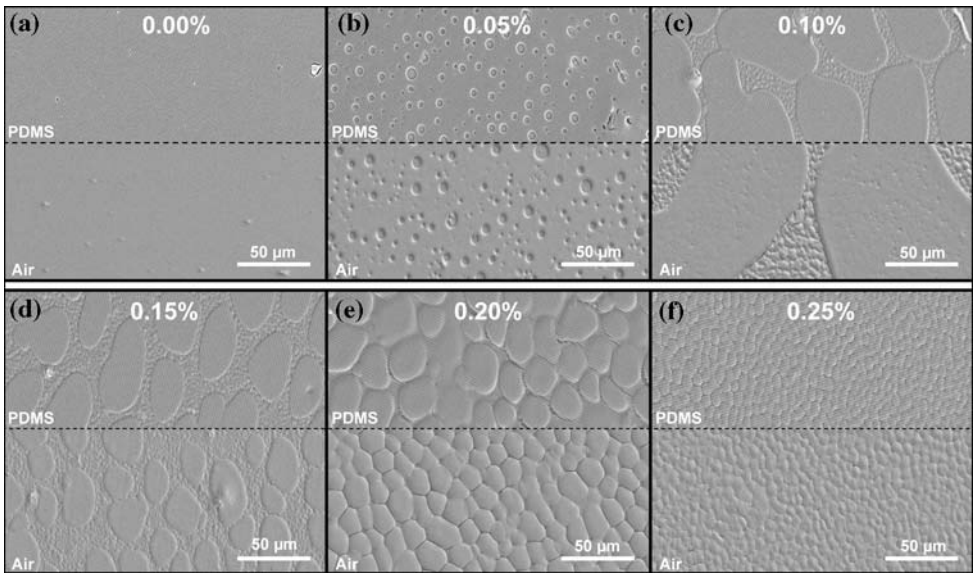

Fig. 10 Surfaces of cast silk/PEO films for various PEO concentrations (as indicated by inset) post-24 h water bath incubation. PDMS and air casting surfaces are indicated by inset. (**a**) No features were formed for the 0% PEO concentration, (**b**) porous void features were formed for the 0.05% PEO concentration, while (**c–f**) globule features were formed for 0.10% and above PEO concentrations

silk film biopolymer matrix. This morphological feature was due to the PEO phase being highly water soluble when compared to the insoluble water-annealed silk fibroin matrix [18]. Additionally, silk films cast with surface patterned features maintained their grooved structures on all film surfaces, although the surface pattern was increasingly disrupted with increasing PEO concentration (Fig. 10a–f). At 0.05 wt./vol.% PEO, porous void features were present on the film surface (Fig. 10b). All other PEO concentrations formed globule-like surface features that corresponded with previously demonstrated silk fibroin assemblies (Fig. 10c–f) [17, 24]. Control films containing no PEO exhibited an absence of defined surface feature formation (Fig. 10a).

Upon closer investigation of the 0.05% PEO pore forming concentration, it was apparent that pore formation exhibited a different morphology than the fibroin aggregates. The porous features were void structures within the film matrix (Fig. 10b). These porous features were likely formed from PEO aggregates that solubilized during the incubation in the water bath. It has been previously shown that PEO will form globules in solution in the presence of other macromolecules [61, 62], such as silk fibroin which is approximately 390 kDa [2]. SEM imaging of the 0.05% PEO silk film surfaces revealed pore sizes between 0.3 and 58.0 μm^2 (Table 4).

PEO concentrations above 0.05% did not demonstrate these porous void features on the silk film surfaces, and were replaced by various sized silk fibroin globules ranging from 0.60 to 458 μm^2 (Fig. 10c–f; Table 4). The lack of porous features indicates that with increased PEO concentration a continuous phase separation occurred throughout the solution as opposed to globular aggregates. PEO concentration also influenced the overall percent silk film surface area occupied by feature formation (Fig. 11a). Below 0.20% PEO concentration surface features were not present over the entire film surface. Lack of uniform dispersion was indicated by the presence of continuous fibroin phases (or large globules) interspaced by regions consisting of smaller fibroin globules (Fig. 11c and d). The continuous fibroin surface area decreased in size with increasing PEO concentration, with a corresponding increase in small fibroin globule surface area (Fig. 11a). At concentrations of 0.20% PEO and above, the entire surface of the silk film was composed of uniformly sized fibroin globules. Increasing PEO concentration beyond 0.20% further reduced the relative surface area of the fibroin globules. These data indicate that the PEO molecules were not capable of uniform dispersion throughout the aqueous phase below a 0.20% concentration during film casting.

Silk film casting interfaces (PDMS and air) resulted in similar feature formation (Fig. 11). ANOVA was performed followed by post hoc Student *t*-tests between different interface group means, and between the means of different group sample sets of similar interfaces. Significant differences in total percent area coverage by surface features were observed between the 0.05% PEO feature formation for different casting interfaces and between all different concentration sample sets (Fig. 11a). Uniform dispersion of PEO within 1% silk fibroin solution was found to occur between 0.15% and 0.20% concentrations for both casting interfaces. This was indicated by complete surface coverage with uniformly sized fibroin globules being reached at 0.20% PEO concentration. Significant differences existed between surface feature size means between the two casting interfaces for all PEO

Table 4 Silk/PEO film surface feature size statistics for both casting interfaces

PEO (%)	Interface	Mean (μm^2)	Standard deviation ($\pm\mu m^2$)	95.0% C.I. ($\pm\mu m^2$)	Median (μm^2)	Range (μm^2)
0.05	PDMS	8.63	13.05	3.00	2.70	57.70
0.05	Air	17.93	18.00	4.14	10.70	78.10
0.10	PDMS	7.85	4.45	1.02	6.80	25.90
0.10	Air	11.39	7.87	1.81	9.70	41.60
0.15	PDMS	27.96	28.20	6.49	22.70	175.20
0.15	Air	10.69	10.24	2.36	7.60	56.10
0.20	PDMS	186.42	105.18	24.20	160.80	419.80
0.20	Air	125.11	65.83	15.15	106.10	281.00
0.25	PDMS	86.48	62.17	14.30	66.40	241.40
0.25	Air	44.94	32.26	7.42	35.40	171.00

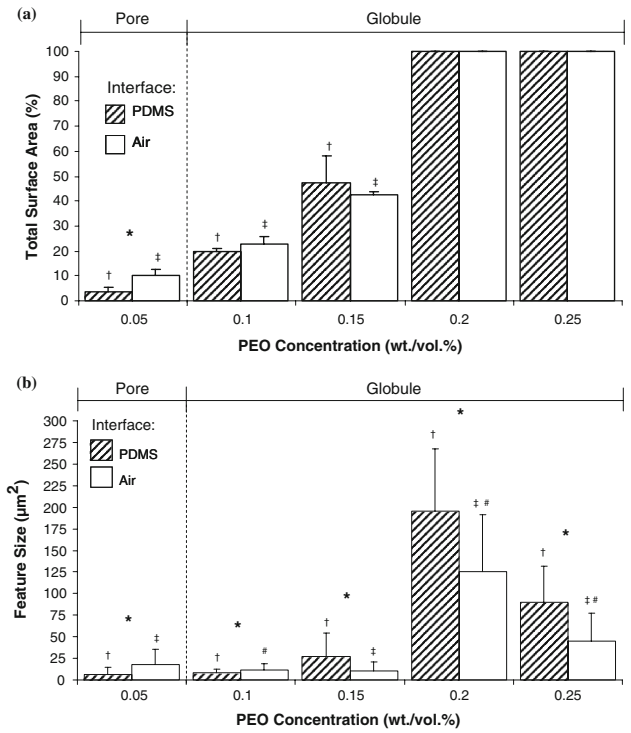

Fig. 11 (**a**) Total surface area of silk/PEO film occupied by surface features for various PEO concentrations. Total film surface area occupied by features increased with increasing PEO concentration. * Indicates statistical difference between different casting interfaces ($n = 3$; $p < 0.05$); ‡ and † indicate statistical differences between sample sets of similar casting interfaces ($p < 0.05$). (**b**) Surface feature area size is modulated by PEO concentration. * Indicates statistically significant difference between means of casting interface groups; #, †, and ‡ indicate statistically significant differences between means of PEO concentrations within similar casting interface groups ($n = 75$; $p < 0.05$; error bars = SD)

concentrations (Fig. 11a). These results indicate that control over surface feature size may also be regulated through interfacial interactions.

Statistically significant differences were also found between the means for all PDMS interface PEO concentrations, indicating that PEO concentration may be selected to produce desired feature sizes (Fig. 11b). For air interface interactions, statistical differences between mean surface areas were found to exist between all PEO concentrations except when comparing 0.10% to both 0.05 and 0.15% PEO concentration feature sizes (Fig. 11b). These results suggest that a potential minimum to fibroin globule feature size formation may exist for dilute PEO concentrations. It is still unclear whether such a minimum exists for pore formation. The above results demonstrate how silk film surface feature morphology, size, and distribution may be controlled by varying PEO concentration within 1% silk solutions. The various feature sizes and accompanying statistical data are summarized in Table 4.

Control of cross-sectional silk film globule size by PEO addition

Silk film samples of approximately 20 μm thickness and varying PEO concentrations were flash frozen in liquid nitrogen and cracked in half using a razor edge. These samples were then imaged under SEM to inspect cross-sectional fibroin globule size. It was found that these globules existed throughout the silk film's cross section (Fig. 12b and c). Control films that did not contain PEO exhibited no globule formation within their cross-sectional area (data not shown). It was observed that with increasing PEO concentration cross-sectional globule size decreased.

Statistical analysis was performed across groups using ANOVA and post hoc Student *t*-tests to compare globule surface area. Statistical difference between mean globule surface areas existed between 0.16% and 0.31%, and between 0.58% and 0.61% PEO concentrations (Fig. 12a). Doubling PEO concentration from 0.16% to 0.32% produced a threefold decrease in mean globule surface area from 6 to 2 μm^2. However, a subsequent doubling in concentration from 0.31% to 0.61% exhibited only a two-fold decrease in mean globule surface area from 2 to

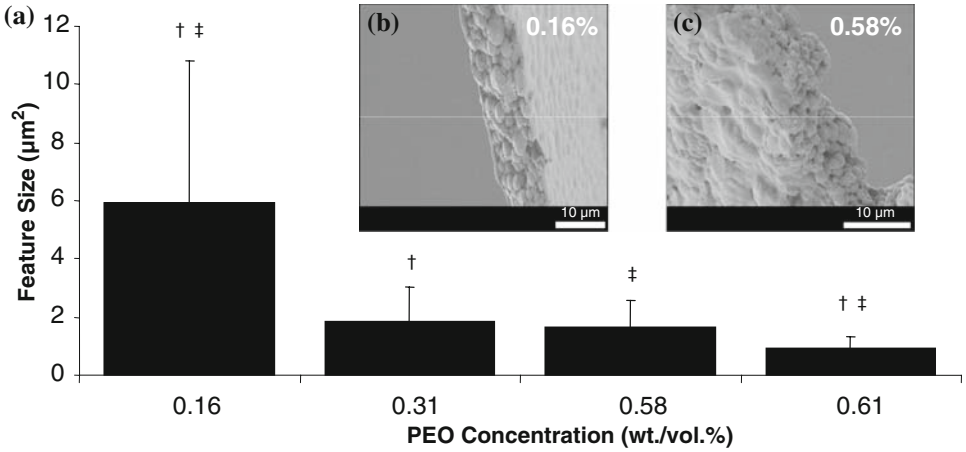

Fig. 12 (**a**) Increasing PEO concentration decreased silk globule formation within film cross-sectional region. † and ‡ indicate statistically significant difference between globule mean surface area for different PEO concentrations ($n = 20$; $p < 0.05$; error bars = SD). SEM images of silk/PEO film cross-sectional areas for (**b**) 0.16% and (**c**) 0.58% PEO concentrations. Globule size decreased and become more densely packed with increasing PEO concentration

1 μm^2. These results indicate that increasing PEO concentration has less impact on decreasing fibroin globule size within the cross-sectional area. However, the standard deviation between the sample sets decreased with increasing PEO concentration. This is best exhibited by a fourfold increase in standard deviation for 0.16% PEO concentration when compared to 0.31% PEO concentration, and a near 10-fold increase for 0.16% PEO when compared to 0.61% (Fig. 12a). These results indicate that increasing PEO concentration produced increased uniformity of silk fibroin globules within the silk film cross section. These results agree with silk film surface feature observations, in which large disparities existed between fibroin globule sizes for 0.15% PEO, while more uniform globule sizes formed with increased PEO concentrations.

Conclusions

Films are a relatively simple 2D structural form generated from silk fibroin solution. However, their structural properties may be fine-tuned to provide predictive biomaterial characteristics [16, 18]. The results from this study demonstrate that control over silk film surface features, thickness, and bulk structure pores can be controlled by predictive inputs such as silk or PEO concentration. The straightforward production techniques for producing these films allows for consistent processing between batches [17]. Silk film thicknesses were found to be consistent over a 500 nm to 50 μm range. Silk film surface feature morphology, size, and distribution can be controlled using soft lithography surface patterning or by adjusting dilute PEO concentrations [17]. Regarding PEO additions, surface morphologies may be altered between pore or globule formation depending on the PEO concentration within 1% silk fibroin solution. As a result, both porous and globular surfaces may be produced using the same basic processing technique.

Silk film biomaterials have potential applicability for a variety of optical and regenerative medicine applications. Transparent and water insoluble silk films can be produced using water-annealing methods [18]. FTIR analysis of silk fibroin secondary structure content after water-annealing indicates that β-sheet secondary structure content increases with proportional decreases in silk I turn structures. The data indicate that water-annealing provides increased β-sheet content within the bulk film structure. In addition, an increase in α-helix structure content was discovered after water-annealing. This effect may be attributed to the increased hydrophobicity of the surrounding environment with increasing β-sheet composition [57]. These results support previous reports that indicated water-annealing promotes β-sheet formation [18, 29]. Water-annealing processing demonstrates how β-sheet content can be modified pending processing condition. Steam sterilization after water-annealing provided an additive effect for inducing β-sheet formation, with corresponding decreases in α-helix content.

The availability of tailored surface features allows for increased design options when using these silk film biomaterials. The added benefit of control of feature size allows for defined production of surfaces that may provide bioactive stimulus to biological systems, as has been reported for other systems. Also, differences exhibited between PDMS and air interfaces allows for the modification of the interface environment to control feature formation. Cross-sectional variability between fibroin globule sizes is largely dictated by PEO concentration. Increasing PEO concentration decreases mean globule surface area while simultaneously increasing globule surface area uniformity. In addition, the effect on decreasing globule size is lessened with increasing PEO concentration. The above results indicate that both surface and bulk feature morphologies may be controlled by adjusting PEO concentration.

The range of available silk film thicknesses allows these biomaterials to be tailored for a selected biological system

from the cellular to organ level. Surface features may be modified to provide bioactive surface signaling to seeded cells to elicit biological outcomes such as cell proliferation, attachment, and motility [32, 38, 40, 41, 63, 64]. Porous silk films could potentially be used in co-cultures studies to separate cell types, but allow for intercellular signaling factors to penetrate between layers and elicit desired cell responses. In addition, potential applications for drug delivery could be explored, along with studies to characterize how biodegradation rates and byproducts are altered with the changes in morphological and structural features reported here.

The range of control over silk film properties teamed with scalable processing techniques offers an expanded set of options for biomaterial design and application. Future studies are needed to define diffusion characteristics and biological responses to the range of surface feature formations. In addition, further studies into the elicited biological response from these silk films will provide more insight into the full utility of these biomaterials. The combined tool set for controlling silk film geometry and bulk structure will provide a foundation for further development of novel silk film biomaterial devices.

Acknowledgements The authors thank the NIH P41 Tissue Engineering Resource Center for support for this work. Additionally, the authors would like to thank Mark Cronin-Golomb for technical assistance with AFM imaging, Xiao Hu for technical assistance with FTIR, and Katherine Chui for providing technical assistance in material processing. This material is based upon work supported in part by the U.S. Army Research Laboratory and the U.S. Army Research Office under contract number W911NF-07-1-0618 and by the DARPA-DSO.

References

1. Altman GH, Diaz F, Jakuba C, Calabro T, Horan RL, Chen J et al (2003) Biomaterials 24(3):401. doi:10.1016/S0142-9612(02)00353-8
2. Vepari C, Kaplan DL (2007) Prog Polym Sci (Oxford) 32(8–9):991. doi:10.1016/j.progpolymsci.2007.05.013
3. Altman GH, Horan RL, Lu HH, Moreau J, Martin I, Richmond JC et al (2002) Biomaterials 23:4131. doi:10.1016/S0142-9612(02)00156-4
4. Meinel L, Fajardo R, Hofmann S, Chen J, Langer R, Snyder B et al (2005) Bone 37:688. doi:10.1016/j.bone.2005.06.010
5. Minoura N, Aiba SI, Gotoh Y, Tsukada M, Imai Y (1995) J Biomed Mater Res 29(10):1215. doi:10.1002/jbm.820291008
6. Kim UJ, Park J, Joo Kim H, Wada M, Kaplan DL (2005) Biomaterials 26(15):2775. doi:10.1016/j.biomaterials.2004.07.044
7. Wang X, Kim HJ, Xu P, Matsumoto A, Kaplan DL (2005) Langmuir 21(24):11335. doi:10.1021/la051862m
8. Kardestuncer T, McCarthy MB, Karageorgiou V, Kaplan D, Gronowicz G (2006) Clin Orthop Relat Res 448:234. doi:108110.1097/01.blo.0000205879.50834.fe
9. Hofmann S, Wong Po Foo CT, Rossetti F, Textor M, Vunjak-Novakovic G, Kaplan DL et al (2006) J Control Release 111(1–2):219. doi:10.1016/j.jconrel.2005.12.009
10. Meinel L, Hofmann S, Karageorgiou V, Kirker-Head C, McCool J, Gronwicz G et al (2005) Biomaterials 26:147. doi:10.1016/j.biomaterials.2004.02.047
11. Panilaitis B, Altman GH, Chen J, Jin HJ, Karageorgiou V, Kaplan DL (2003) Biomaterials 24(18):3079. doi:10.1016/S0142-9612(03)00158-3
12. Vunjak-Novakovic G, Altman G, Horan R, Kaplan DL (2004) Annu Rev Biomed Eng 6:131. doi:10.1146/annurev.bioeng.6.040803.140037
13. Arai T, Freddi G, Innocenti R, Tsukada M (2004) J Appl Polym Sci 91:2383. doi:10.1002/app.13393
14. Horan RL, Antle K, Collette AL, Wang Y, Huang J, Moreau JE et al (2004) Biomaterials 26:3385. doi:10.1016/j.biomaterials.2004.09.020
15. Horan RL, Antle K, Collette AL, Wang Y, Huang J, Moreau JE et al (2005) Biomaterials 26(17):3385. doi:10.1016/j.biomaterials.2004.09.020
16. Tsukada M, Gotoh Y, Nagura M, Minoura N, Kasai N, Freddi G (1994) J Polym Sci Part Polym Phys 32(5):961. doi:10.1002/polb.1994.090320519
17. Jin H-J, Park J, Valluzzi R, Cebe P, Kaplan DL (2004) Biomacromolecules 5:711. doi:10.1021/bm0343287
18. Jin H-J, Park J, Karageorgiou V, Kim U-J, Valluzzi R, Cebe P et al (2005) Adv Funct Mater 15:1241. doi:10.1002/adfm.200400405
19. Matsumoto A, Chen J, Collette AL, Kim UJ, Altman GH, Cebe P et al (2006) J Phys Chem B 110(43):21630. doi:10.1021/jp056350v
20. Wang X, Kluge JA, Leisk GG, Kaplan DL (2008) Biomaterials 29(8):1054. doi:10.1016/j.biomaterials.2007.11.003
21. Wilson D, Valluzzi R, Kaplan D (2000) Biophys J 78(5):2690
22. Tretinnikov ON, Tamada Y (2001) Langmuir 17(23):7406. doi:10.1021/la010791y
23. Motta A, Fambri L, Migliaresi C (2002) Macromol Chem Phys 203(10–11):1658. doi:10.1002/1521-3935(200207)203:10/11<1658::AID-MACP1658>3.0.CO;2-3
24. Jin H-J, Kaplan DL (2003) Nature 424(28):1057. doi:10.1038/nature01809
25. Hu X, Kaplan DL, Cebe P (2006) Macromolecules 39:6161. doi:10.1021/ma0610109
26. Park J (2004) Structure and properties of silk fibroin films. Diss. Tufts University, Medford, p 56
27. Agarwal K, Hoagland DA, Farris RJ (1997) J Appl Polym Sci 63(3):401. doi:10.1002/(SICI)1097-4628(19970118)63:3<401::AID-APP17>3.0.CO;2-2
28. Xia Y, Whitesides GM (1998) Annu Rev Mater Sci 28(1):153. doi:10.1146/annurev.matsci.28.1.153
29. Lawrence BD, Cronin-Golomb M, Georgakoudi I, Kaplan D, Omenetto FG (2008) Biomacromolecules 9(4):1214. doi: 10.1021/bm701235f
30. Dunn GA, Brown AF (1986) J Cell Sci 83:313
31. Kane RS, Takayama S, Ostuni E, Ingber DE, Whitesides GM (1999) Biomaterials 20(23–24):2363. doi:10.1016/S0142-9612(99)00165-9
32. Teixeira AI, Nealey PF, Murphy CJ (2004) J Biomed Mater Res A 71(3):369. doi:10.1002/jbm.a.30089
33. Liliensiek SJ, Campbell S, Nealey PF, Murphy CJ (2006) J Biomed Mater Res A 79(1):185. doi:10.1002/jbm.a.30744
34. Gupta MK, Khokhar SK, Phillips DM, Sowards LA, Drummy LF, Kadakia MP et al (2007) Langmuir 23(3):1315. doi:10.1021/la062047p
35. Suh KY, Khademhosseini A, Yang JM, Eng G, Langer R (2004) Adv Mater 16(7):584
36. Crabb RAB, Chau EP, Evans MC, Barocas VH, Hubel A (2006) Tissue Eng 12(6):1565. doi:10.1089/ten.2006.12.1565

37. Abrams GA, Schaus SS, Goodman SL, Nealey PF, Murphy CJ (2000) Cornea 19(1):57. doi:10.1097/00003226-200001000-00012
38. Diehl KA, Foley JD, Nealey PF, Murphy CJ (2005) J Biomed Mater Res A 75(3):603. doi:10.1002/jbm.a.30467
39. Karlon WJ, Hsu PP, Song LI, Chien S, McCulloch AD, Omens JH (1999) Ann Biomed Eng 27(6):712. doi:10.1114/1.226
40. Karuri NW, Liliensiek S, Teixeira AI, Abrams G, Campbell S, Nealey PF et al (2004) J Cell Sci 117(15):3153. doi:10.1242/jcs.01146
41. Karuri NW, Porri TJ, Albrecht RM, Murphy CJ, Nealey PF (2006) IEEE Trans Nanobiosci 5(4):273. doi:10.1109/TNB.2006.886570
42. ImageJ, Wayne Rasband. National Institute of Health, USA
43. Arrondo JLR, Muga A, Castresana J, Goñi FM (1993) Prog Biophys Mol Biol 59(1): 23. doi:10.1016/0079-6107(93)90006-6
44. Dong A, Huang P, Caughey WS (1990) Biochemistry 29(13): 3303. doi:10.1021/bi00465a022
45. Speare JO, Rush TS III (2003) Biopolymers 72(3):193. doi:10.1002/bip.10337
46. 1.37C, I.V., Wayne Rasband. National Institute of Health, USA
47. Vollrath F, Knight DP (2001) Nature 410(6828):541. doi:10.1038/35069000
48. Valluzzi R, Jin HJ (2004) Biomacromolecules 5(3):696. doi:10.1021/bm0343085
49. Dongbin Zhao YLZZ (2007) Water 35(1):42
50. Smith CK, Regan L (1997) Acc Chem Res 30(4):153. doi:10.1021/ar9601048
51. Jung C (2000) J Mol Recognit 13(6):325. doi:10.1002/1099-1352(200011/12)13:6<325::AID-JMR507>3.0.CO;2-C
52. Chen X, Shao Z, Marinkovic NS, Miller LM, Zhou P, Chance MR (2001) Biophys Chem 89(1):25. doi:10.1016/S0301-4622(00)00213-1
53. Chen X, Shao Z, Knight DP, Vollrath F (2007) Proteins 68(1):223. doi:10.1002/prot.21414
54. Hu X, Kaplan D, Cebe P (2007) Thermochim Acta 461(1–2):137. doi:10.1016/j.tca.2006.12.011
55. Valluzzi R, Szela S, Avtges P, Kirschner D, Kaplan D (1999) J Phys Chem B 103(51):11382. doi:10.1021/jp991363s
56. Asakura T, Kuzuhara A, Tabeta R, Saito H (1985) Macromolecules 18(10):1841. doi:10.1021/ma00152a009
57. Fink AL (1998) Fold Des 3(1). doi:10.1016/S1359-0278(98)00005-4
58. Mears DR, Pae KD, Sauer JA (1969) J Appl Phys 40(11):4229. doi:10.1063/1.1657180
59. Nakafuku C (1993) Polymer Communications 34(19):4166. doi:10.1016/0032-3861(93)90684-3
60. Nakafuku C, Nishimura K (2003) J Appl Polym Sci 87(12):1962. doi:10.1002/app.11601
61. Cuniberti C, Ferrando R (1972) Polymer (Guildf) 13(8):379. doi:10.1016/0032-3861(72)90058-4
62. Hammouda B, Ho DL, Kline S (2004) Macromolecules 37(18):6932. doi:10.1021/ma049623d
63. Fitton JH, Dalton BA, Beumer G, Johnson G, Griesser HJ, Steele JG (1998) J Biomed Mater Res 42(2):245–257. doi:10.1002/(SICI)1097-4636(199811)42:2<245::AID-JBM9>3.0.CO;2-P
64. Loesberg WA, te Riet J, van Delft FCMJM, Schön P, Figdor CG, Speller S, van Loon JJWA, Walboomers XF, Jansen JA (2007) Biomaterials 28(27):3944. doi:10.1016/j.biomaterials.2007.05.030